Jurnal Ilmu Fisika
Vol. 18, No. 2, September 2026, pp. 158–168
ISSN: 1979-4657 (Print); 2614-7386 (Online)
https://doi.org/10.25077/jif.18.2.158-168.2026

Jurnal Ilmu Fisika
Open Access

Optical Absorption Line Shape of a Λ-Type Three-Level Semiconductor Quantum Dot: Roles of Transition Dipole Moment and Relaxation Rate

Bintoro S. Nugroho, Arik Ramadhan, Asifa Asri

Department of Physics, Faculty of Mathematical and Natural Sciences, Universitas Tanjungpura, Pontianak, 78115, Indonesia

Article Info

Article History:

Received March 27, 2026
Revised July 16, 2026
Accepted August 28, 2026
Published online September 1, 2026

Keywords:

absorption spectrum
density matrix
relaxation rate
semiconductor quantum dot
three-level Λ system

Corresponding Author:

Bintoro S. Nugroho,
Email:
b.s.nugroho@physics.untan.ac.id

ABSTRACT

The optical absorption of an isolated Λ-type three-level semiconductor quantum dot under continuous-wave excitation was investigated theoretically using a semiclassical density-matrix approach. The equations of motion were derived from the master equation within the rotating-wave approximation and solved in the steady-state regime to obtain the optical susceptibility and absorption spectrum. The roles of the transition dipole moment and relaxation rate were examined systematically in both weak- and strong-field regimes. In the weak-field regime, the spectrum was dominated by the $|1\rangle \leftrightarrow |3\rangle$ transition, while a weaker secondary feature associated with the $|2\rangle \leftrightarrow |3\rangle$ transition emerged through relaxation-assisted population redistribution. Increasing the relaxation rate broadened and suppressed the dominant peak, whereas increasing the transition dipole moment mainly broadened the weaker secondary feature. In the strong-field regime, the two absorption channels merged into a broadened composite profile due to the combined effects of stronger coherent driving, power broadening, and relaxation. These results clarify how transition strength and dissipation govern the absorption line shape of an elementary multilevel semiconductor quantum-dot system.

Copyright © 2026 Author(s)

1. INTRODUCTION

Since their first successful synthesis, semiconductor quantum dots (SQDs) have attracted considerable attention because quantum confinement endows them with optical and electronic properties that differ fundamentally from those of bulk semiconductors. When the dot diameter is reduced to the nanometer scale, typically about 2–10 nm, the carrier motion becomes spatially confined, producing discrete energy structures and making the transition energies strongly dependent on size and shape (Alivisatos, 1996; Osypiw et al., 2022). This tunability has made SQDs promising building blocks for a wide range of photonic and optoelectronic applications, including light-emitting devices (Shen et al., 2019; Ollivier et al., 2020), solar cells (Pan et al., 2018), and photodiodes (Pang et al., 2024). Beyond these applications, SQDs have also been intensively explored for sensing (Chen et al., 2018), bioimaging (Martynenko et al., 2017), phototherapy (Guo et al., 2024), and photocatalysis (Gui et al., 2024). Their broad applicability is rooted in the fact that their optical response can be engineered through structural design, material composition, and external excitation.

Among the various optical characteristics of SQDs, the absorption spectrum is particularly important because it directly reflects the accessible electronic transitions and their coupling to incident radiation. In practical terms, the absorption spectrum provides insight into the electronic structure of the

Attribution-NonCommercial 4.0 International

dot, the excitation pathways involved, and the underlying carrier dynamics (Pokutnyi et al., 2016; Holtkemper et al., 2018). The spectral response is also highly sensitive to external perturbations, including applied electric, magnetic, or optical fields, which further enhances its utility as a probe of controllable light-matter interaction in confined semiconductor systems (Yücel et al., 2022; Toscano-Negrette et al., 2023). A clear understanding of the absorption behavior is therefore essential not only from a fundamental perspective, but also for improving the performance of SQD-based nanophotonic and optoelectronic devices such as sensors, imaging platforms, and energy-conversion systems (Yin et al., 2018; Maiti et al., 2019; Deng et al., 2020; Foerster & Besley, 2022). In addition, the importance of analyzing optical response at the single-dot level has been increasingly emphasized because single-quantum-dot spectroscopy can reveal intrinsic excitonic dynamics that are often masked in ensemble measurements (Li et al., 2024).

In addition to isolated dots, SQDs can be arranged into ordered assemblies whose collective optical behavior is substantially richer than that of individual emitters. In such systems, lattice geometry, inter-dot interaction, and collective excitonic effects introduce additional degrees of freedom that can modify the optical response in nontrivial ways (Marino et al., 2020; Ondry et al., 2021). Previous studies have reported a variety of remarkable phenomena in coupled or structured quantum-dot systems, including nonlinear optical response, supercrystal excitonic effects, and quantum metasurface behavior in arrays of multi-level emitters (Vovk et al., 2018; Ryzhov et al., 2019, 2021). Related theoretical work has also shown that the optical response of quantum-dot-based nanostructures can be strongly altered by geometrical factors, further highlighting the sensitivity of such systems to structural and interaction parameters (Nugroho & Yulyanto, 2020). However, a physically reliable interpretation of these more complex systems requires a firm understanding of the optical response at the single-emitter level. In this context, the isolated SQD should not be viewed merely as a simplified model, but as the elementary unit from which the optical physics of more complex multi-dot architectures must be understood.

A particularly instructive minimal model is the isolated Λ-type three-level SQD. Unlike the conventional two-level picture, a Λ-type configuration contains two optically allowed transitions coupled to a common upper state. As a result, its absorption spectrum is governed not only by the resonance condition of each transition, but also by the competition between excitation pathways, their relative transition strengths, and relaxation-induced population redistribution among the participating states. Such a configuration therefore provides a simple but physically meaningful setting for examining how multilevel structure modifies the steady-state optical response of an SQD beyond the standard two-level description. More importantly, Λ-type three-level systems are widely recognized as a fundamental setting for quantum-interference-driven optical phenomena such as electromagnetically induced transparency, coherent population trapping, and related nontrivial spectral behavior (Bayrakli, 2021). This means that even at the single-emitter level, the Λ configuration already contains essential multilevel physics that is absent in a simple two-level description.

Despite its physical relevance, the optical absorption of an isolated Λ-type three-level SQD under continuous-wave (CW) excitation has not yet been fully explored. In particular, the individual and combined effects of the transition dipole moment and the relaxation rate on the height, width, and spectral position of the absorption features have not yet been articulated clearly for this elementary configuration. This point is important because these two parameters directly govern how strongly the SQD couples to the external field and how rapidly the excited population relaxes, thereby controlling the competition between excitation and dissipation in the steady-state optical response. A focused study of this isolated Λ-type system is therefore needed not only to establish the intrinsic absorption mechanisms of a representative multilevel SQD, but also to provide a reliable conceptual basis for interpreting more complex coupled, driven, or collectively interacting quantum-dot systems.

In this work, we theoretically investigate the optical absorption of an isolated Λ-type three-level SQD under continuous-wave excitation. The optical response is formulated within the density-matrix approach under the rotating-wave approximation, while population relaxation is incorporated through the Lindblad operator. Particular emphasis is placed on identifying how the transition dipole moment and the relaxation rate shape the absorption spectrum in the weak- and strong-field regimes. By systematically separating and comparing the effects of these parameters, this study aims to clarify the

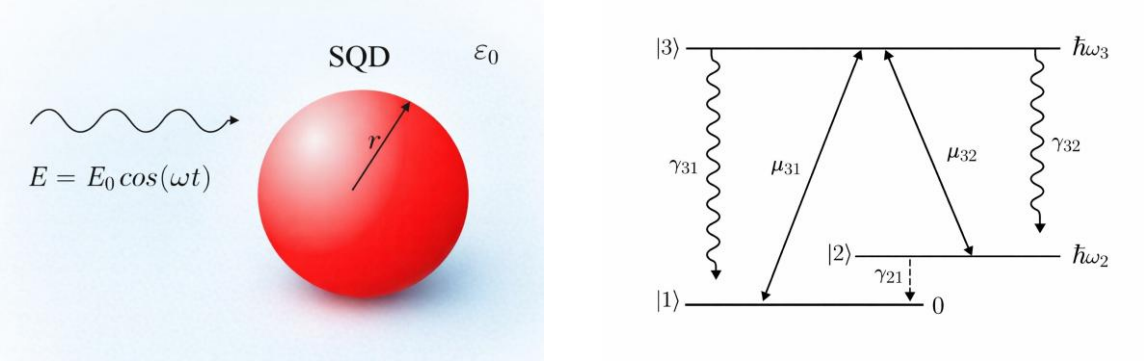
physical mechanisms that govern the absorption line shape of a simple but representative multilevel SQD system and to provide a useful baseline for interpreting more complex quantum-dot structures.

2. METHOD

To investigate the optical absorption of an isolated Λ-type three-level SQD, we formulate the system dynamics using the density-matrix master equation under CW optical excitation. The equations of motion for the density-matrix elements are obtained by projecting the master equation onto the basis states of the three-level system. The steady-state solution is then determined by setting all time derivatives to zero, which reduces the dynamical problem to a system of linear algebraic equations. The resulting steady-state coherences are subsequently used to calculate the electric susceptibility and the absorbed optical power, from which the absorption spectrum is obtained.

2.1 Theoretical Model of the Λ-Type Three-Level System

The system considered in this work is shown schematically in Figure 1(a). It consists of an isolated spherical SQD of radius r, embedded in vacuum with permittivity ε_0, and driven by a linearly polarized monochromatic electric field $E(t) = E_0\cos(\omega t)$, where $E_0$and ω denote the amplitude and angular frequency of the incident field, respectively. Since the SQD size is assumed to be much smaller than the optical wavelength, $r \ll \lambda$, the spatial variation of the external field across the dot can be neglected. Accordingly, the field is treated as spatially uniform inside the SQD within the quasistatic approximation, and the light-matter interaction is described within the electric-dipole approximation.



(a) (b)

Figure 1 (a) Schematic of the isolated semiconductor quantum dot driven by a linearly polarized monochromatic electric field. (b) Energy-level diagram of the Λ-type three-level system. The wavy arrows denote spontaneous decay from the upper state to the lower states, while the dashed arrow denotes relaxation between the two lower states.

The SQD is modeled as a Λ-type three-level quantum system with basis states $|1\rangle$, $|2\rangle$, and $|3\rangle$, having energies 0, $\hbar\omega_2$, and $\hbar\omega_3$, respectively, as illustrated in Figure 1(b). The optically allowed transitions are $|1\rangle \leftrightarrow |3\rangle$and $|2\rangle \leftrightarrow |3\rangle$, characterized by the transition dipole moments $\mu_{31}(=\mu_{13})$ and $\mu_{32}(=\mu_{23})$. For simplicity, both transition dipole moments are assumed to be parallel to each other and to the polarization direction of the incident field, so that the vector quantities can be treated as scalars.

Relaxation is incorporated through spontaneous decay from the upper state $|3\rangle$ to the lower states $|1\rangle$ and $|2\rangle$, with decay rates γ_{31} and γ_{32}, respectively. In addition, population relaxation from $|2\rangle$ to $|1\rangle$ is included through the rate γ_{21}. In the present formulation, the Lindblad terms are restricted to population relaxation channels, whereas additional pure-dephasing processes that directly damp the optical coherences without changing the level populations are not included explicitly. Within this framework, the model retains the essential coherent and dissipative processes needed to examine how transition strength and relaxation channels shape the absorption response of an isolated Λ-type SQD under CW driving.

2.2 Density-Matrix Equations of Motion

The optical response of the SQD is described using the density-matrix formalism. Under the rotating-wave approximation (RWA), the system dynamics are governed by the master equation (Ryzhov et al., 2021)

$$\dot{\hat{\rho}} = -\frac{i}{\hbar}\left[\hat{\mathcal{H}}^{\mathrm{RWA}}, \hat{\rho}\right] + \hat{\mathcal{L}}(\hat{\rho}), \tag{1a}$$

where

$$\hat{\mathcal{H}}^{RWA} = \hbar(\Delta_{21}\hat{\sigma}_{22} + \Delta_{31}\hat{\sigma}_{33}) - \frac{\hbar}{2}(\Omega_{31}\hat{\sigma}_{31} + \Omega_{32}\hat{\sigma}_{32} + H.c.), \tag{1b}$$

is the Hamiltonian in the rotating frame and

$$\begin{aligned}\hat{\mathcal{L}}(\hat{\rho}) = \frac{1}{2}\gamma_{31}([\hat{\sigma}_{13}\hat{\rho}, \hat{\sigma}_{31}] + [\hat{\sigma}_{13}, \hat{\rho}\hat{\sigma}_{31}]) + \frac{1}{2}\gamma_{32}([\hat{\sigma}_{23}\hat{\rho}, \hat{\sigma}_{32}] + [\hat{\sigma}_{23}, \hat{\rho}\hat{\sigma}_{32}]) \\ + \frac{1}{2}\gamma_{21}([\hat{\sigma}_{12}\hat{\rho}, \hat{\sigma}_{21}] + [\hat{\sigma}_{12}, \hat{\rho}\hat{\sigma}_{21}]).\end{aligned} \tag{1c}$$

is the Lindblad operator describing the radiation relaxation of the SQD states. Here, the overdot denotes the time derivative, $[\hat{O}_1, \hat{O}_2]$ denotes the commutator, and $\hat{\sigma}_{nm} = |n\rangle\langle m|$ with $m, n = 1, 2, 3$ is the transition operator between basis states. The quantity $\hbar\Delta_{21} = \hbar(\omega_2 - \omega_1)$ represents the energy splitting between the two lower states, while $\hbar\Delta_{31} = \hbar\omega_3 - \hbar\omega$ is the detuning of the incident field from the $|1\rangle \leftrightarrow |3\rangle$ transition, $\Omega_{31} = \mu_{31}E_0/\hbar$ and $\Omega_{32} = \mu_{32}E_0/\hbar$ are the Rabi frequencies associated with the $|1\rangle \leftrightarrow |3\rangle$ and $|2\rangle \leftrightarrow |3\rangle$ transitions, respectively, and H.c. denotes the Hermitian conjugate.

Projecting Eq. (1a) onto the basis states, $\rho_{nm} = \langle n|\hat{\rho}|m\rangle$, yields the equations of motion for the density-matrix elements:

$$\dot{\rho}_{11} = \frac{i\Omega_{31}}{2}(\rho_{31} - \rho_{13}) + \gamma_{21}\rho_{22} + \gamma_{31}\rho_{33}, \tag{2a}$$

$$\dot{\rho}_{22} = \frac{i\Omega_{32}}{2}(\rho_{32} - \rho_{23}) - \gamma_{21}\rho_{22} + \gamma_{32}\rho_{33}, \tag{2b}$$

$$\dot{\rho}_{33} = -\frac{i\Omega_{31}}{2}(\rho_{31} - \rho_{13}) - \frac{i\Omega_{32}}{2}(\rho_{32} - \rho_{23}) - \rho_{33}(\gamma_{31} + \gamma_{32}), \tag{2c}$$

$$\dot{\rho}_{31} = -\left[i\Delta_{31} + \frac{1}{2}(\gamma_{31} + \gamma_{32})\right]\rho_{31} + \frac{i\Omega_{32}}{2}\rho_{21} - \frac{i\Omega_{31}}{2}(\rho_{33} - \rho_{11}), \tag{2d}$$

$$\dot{\rho}_{32} = -\left[i(\Delta_{31} - \Delta_{21}) + \frac{1}{2}(\gamma_{31} + \gamma_{32} + \gamma_{21})\right]\rho_{32} + \frac{i\Omega_{31}}{2}\rho_{12} - \frac{i\Omega_{32}}{2}(\rho_{33} - \rho_{22}), \tag{2e}$$

$$\dot{\rho}_{21} = \frac{i\Omega_{32}}{2}\rho_{31} - \frac{i\Omega_{31}}{2}\rho_{23} - \left(i\Delta_{21} + \frac{1}{2}\gamma_{21}\right)\rho_{21}. \tag{2f}$$

These coupled equations describe the time evolution of the state populations and quantum coherences under the combined action of coherent optical driving and relaxation.

2.3 Steady State Solution of Equation of Motion

To determine the optical absorption spectrum under continuous-wave excitation, the density-matrix equations are solved in the steady-state regime by imposing $\dot{\rho}_{mn} = 0$ for all density-matrix elements appearing in Eqs. (2a)-(2f). Under this condition, the transient dynamics vanish and the system response becomes time-independent, even though the SQD remains continuously driven by the external field. Consequently, Eqs. (2a)–(2f) are reduced from a set of coupled first-order differential equations to a set of linear algebraic equations.

The steady-state equations are solved together with the normalization condition,

$$\rho_{11} + \rho_{22} + \rho_{33} = 1, \tag{3}$$

which expresses conservation of the total population. One of the diagonal equations is therefore replaced by this normalization relation, and the resulting set of equations is arranged in the matrix form

$$\mathbf{MR} = \mathbf{B}, \tag{4}$$

where **M** is the coefficient matrix containing the coefficients of the steady-state density-matrix equations, **R** is the vector of unknown density-matrix elements, and **B** is the corresponding constant vector. For each excitation frequency and parameter set, the steady-state density-matrix elements are obtained by numerically solving this linear system. The resulting linear algebraic system was solved using an in-house Python code with a direct linear solver from the NumPy library. For each excitation frequency and parameter set, the steady-state density-matrix elements were obtained from this linear system. All graphs were generated using the Matplotlib library. As a numerical consistency check, the population-normalization condition [Eq. (3)] was verified at each frequency point.

2.4 Susceptibility and Absorbed Energy

After the steady-state density-matrix elements have been obtained, the coherences associated with the optically allowed transitions are used to evaluate the electric susceptibility,

$$\chi = \frac{2}{\varepsilon_0 V_{SQD} E_0}(\mu_{31}\rho_{31} + \mu_{32}\rho_{32}), \tag{5}$$

where V_{SQD} is the SQD volume. Because the induced polarization is determined by the transition coherences, the susceptibility directly reflects the steady-state optical response of the driven three-level system. The optical absorption is then identified from the imaginary part of the susceptibility.

The average absorbed power Q is evaluated from the standard relation (Yariv, 1989)

$$Q = \frac{1}{2}\omega\varepsilon_0 \mathrm{Im}(\chi)|E_0|^2 V_{SQD}. \tag{6}$$

so that, for each excitation frequency, the absorption spectrum is obtained consistently from the steady-state solution of the density-matrix equations. In this way, the numerical procedure links the microscopic coherences of the SQD directly to the macroscopic absorption response.

Unless otherwise stated, the model parameters are fixed at $\hbar\Delta_{21} = 0.6$ meV, $\mu_{31} = 0.5e$ nm, $\gamma_{31} = 3\ \mathrm{ns}^{-1}$, and $\gamma_{21} = 0.01\gamma_{31}$, where e is the elementary charge. The quantities μ_{32} and γ_{32} are treated as control parameters to examine, respectively, the roles of relaxation and transition strength in shaping the absorption spectrum. Throughout this work, γ_{31} and μ_{31} are used as normalization units for quantities with dimensions of frequency and dipole moment, respectively.

3. RESULTS AND DISCUSSION

The optical absorption of the isolated semiconductor quantum dot (SQD) is analyzed in two excitation regimes, namely weak- and strong-field excitation. In the weak-field regime, the calculation is intended to reveal the near-linear spectral response and to distinguish the relative contribution of each optically allowed transition. In the strong-field regime, the calculation is used to examine how stronger optical driving modifies the spectral profile through enhanced coupling, power broadening, and stronger competition between the two excitation pathways. In both regimes, the relaxation rate γ_{32} and the transition dipole moment μ_{32} are varied systematically to control, respectively, the dissipation strength and the light-matter interaction strength. In addition, the splitting energy Δ_{21} is varied separately to verify the physical origin of the secondary absorption feature, since this parameter directly determines the spectral separation between the two optical transitions. This is also physically relevant because the splitting energy can depend on the surrounding conditions of the system (Ryzhov et al., 2021).

Figure 2 shows the optical absorption spectrum in the weak-field regime for several values of the relaxation rate γ. Figures 2(a)-(c) correspond to $\mu_{32} = 0.3\mu_{31}$, $\mu_{32} = \mu_{31}$, and $\mu_{32} = 3\mu_{31}$, respectively. In all three panels, the spectrum is dominated by a primary peak located near $\hbar\Delta_{31} = 0$, indicating that the absorption is governed mainly by the $|1\rangle \leftrightarrow |3\rangle$ transition under weak excitation. This dominant feature is clearly observed in Figures 2(a)-2(c), where the largest peak consistently appears around the resonance condition of the $|1\rangle \leftrightarrow |3\rangle$ transition. As γ_{32} increases within each panel, this main peak becomes broader and lower. The broadening is consistent with lifetime broadening, since a larger relaxation rate shortens the effective lifetime of the excited state and consequently increases the homogeneous linewidth. By contrast, the reduction in peak height is more appropriately interpreted as a steady-state population redistribution effect. Faster relaxation reduces the effective population difference that supports the $|1\rangle \leftrightarrow |3\rangle$ absorption channel, thereby weakening the dominant resonance.

In addition to the main resonance, Figures 2(a)–2(c) also exhibit a weaker secondary peak near $\hbar\Delta_{31} = 0.6$ meV, as highlighted in the inset of Figure 2. This feature is much smaller than the primary one and becomes visible only under certain parameter combinations, indicating that the $|2\rangle \leftrightarrow |3\rangle$ channel does not dominate the weak-field response. Physically, this behavior suggests that a small fraction of the population is first transferred to the upper state even when the excitation is not tuned to the second transition. Part of this excited population is then redistributed to state $|2\rangle$ through relaxation, allowing the $|2\rangle \leftrightarrow |3\rangle$ transition to contribute to the steady-state absorption when the excitation frequency approaches its resonance. Therefore, the secondary peak can be understood as a weaker relaxation-assisted absorption channel superimposed on the dominant $|1\rangle \leftrightarrow |3\rangle$ response.

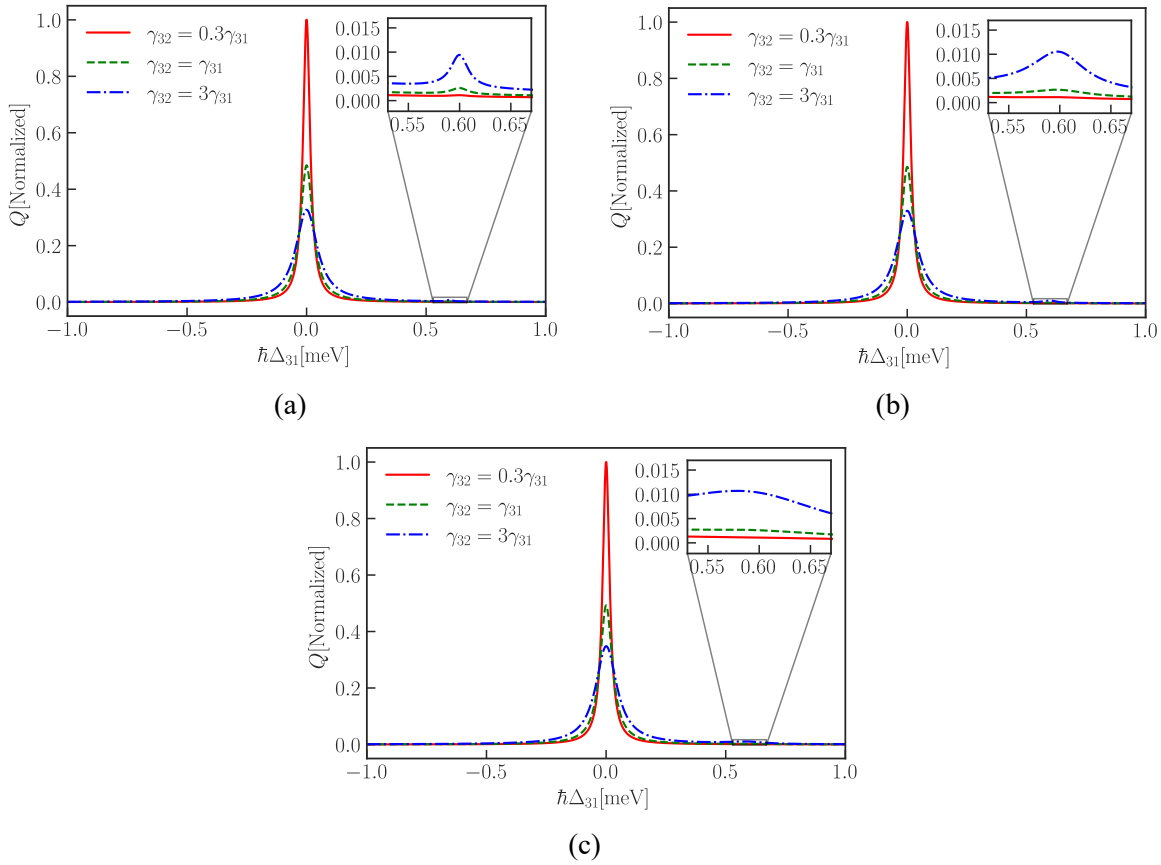


Figure 2. Optical absorption spectrum in the weak-field regime for $\Omega_{31} = 10^{0.5}\,\gamma_{31}$. Panels (a), (b), and (c) correspond to $\mu_{32} = 0.3\mu_{31}$, $\mu_{32} = \mu_{31}$, and $\mu_{32} = 3\mu_{31}$, respectively. In each panel, the curves represent different values of γ_{32}. The inset shows a zoomed-in view of the weak secondary peak associated with the $|2\rangle \leftrightarrow |3\rangle$ transition.

To verify this interpretation, an additional control calculation was performed by setting $\gamma_{32} = 0$ while keeping the other parameters unchanged. The result, not shown here, indicates that the secondary feature near $\hbar\Delta_{31} \approx \Delta_{21}$ is strongly suppressed in the absence of this relaxation channel, whereas the dominant $|1\rangle \leftrightarrow |3\rangle$ resonance remains visible. This behavior confirms that the secondary peak is not generated solely by the resonance condition of the $|2\rangle \leftrightarrow |3\rangle$ transition. Instead, it requires population redistribution into state $|2\rangle$ through relaxation from the upper state $|3\rangle$, so that the $|2\rangle \leftrightarrow |3\rangle$ transition can contribute to the steady-state absorption.

A more specific effect of the transition dipole moment can be identified by comparing Figures 2(a), 2(b), and 2(c). Over the range considered here, the primary peak changes only modestly from Figure 2(a) to Figure 2(c), indicating that the dominant $|1\rangle \leftrightarrow |3\rangle$ resonance remains controlled mainly by the resonance condition and relaxation-induced linewidth rather than by a moderate increase in coupling strength. In contrast, the secondary peak becomes broader as μ_{32} increases, which is most evident when comparing the relatively sharper secondary structure in Figure 2(a) with the broader feature in Figures 2(b) and 2(c). Since the Rabi frequency is proportional to the transition dipole moment, a larger μ_{32} strengthens the optical coupling and partially relaxes the suppression of the off-resonant $|2\rangle \leftrightarrow |3\rangle$ pathway. As a result, the weaker transition contributes to the absorption over a wider frequency interval, which appears as a broadening of the secondary spectral feature. These results indicate that, under weak excitation, the relaxation rate mainly controls the linewidth and amplitude of the dominant peak, whereas the transition dipole moment more clearly affects the accessibility of the weaker transition channel.

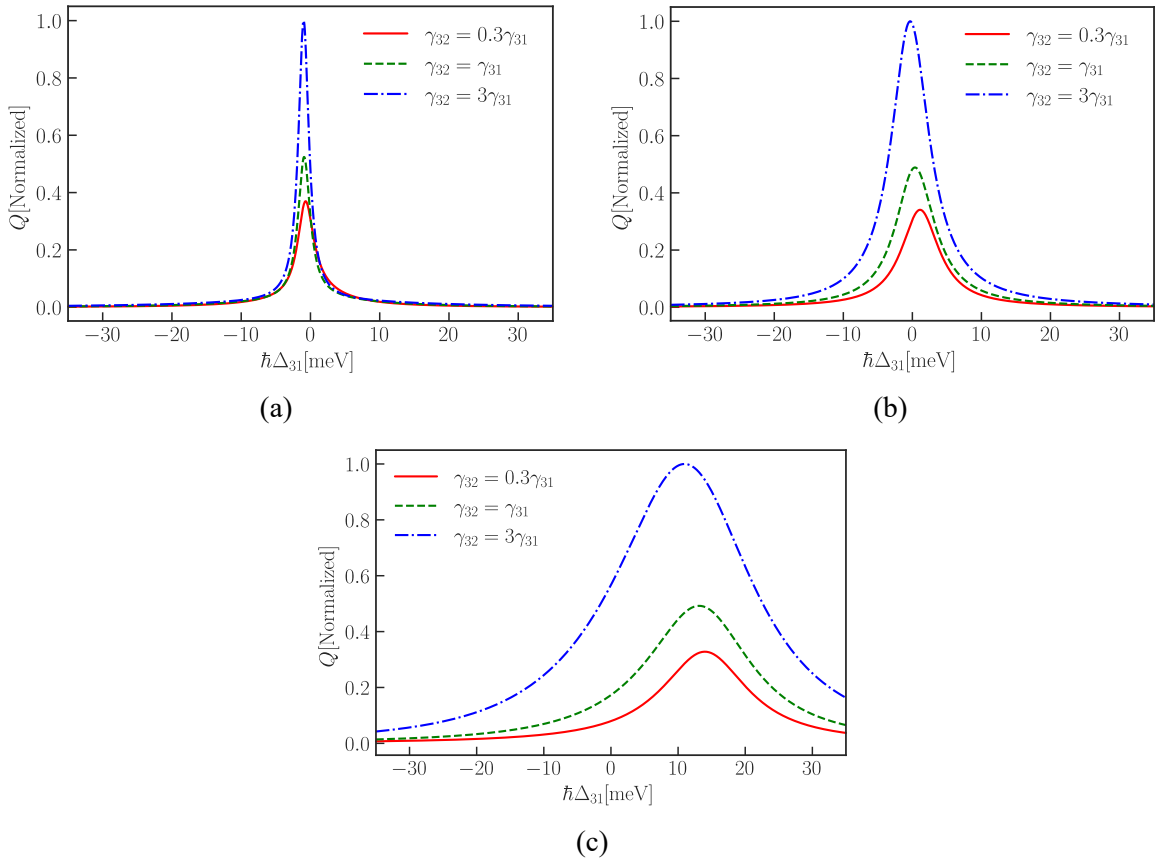


Figure 3. Optical absorption spectrum in the strong-field regime for $\Omega_{31} = 10^3\ \gamma_{31}$. Panels (a), (b), and (c) correspond to $\mu_{32} = 0.3\mu_{31}$, $\mu_{32} = \mu_{31}$, and $\mu_{32} = 3\mu_{31}$, respectively. In each panel, the curves represent different values of γ_{32}. Other parameters are the same as those used in Figure 2.

Figure 3 presents the absorption spectrum in the strong-field regime under the same variation conditions as in Figure 2. Figures 3(a)-(c) correspond to $\mu_{32} = 0.3\mu_{31}$, $\mu_{32} = \mu_{31}$, and $\mu_{32} = 3\mu_{31}$,

respectively. In contrast to the weak-field case shown in Figures 2(a)-2(c), the spectrum in Figures 3(a)-3(c) exhibits a single broadened structure rather than two clearly separated peaks. This behavior indicates that the resonances associated with the $|1\rangle \leftrightarrow |3\rangle$ and $|2\rangle \leftrightarrow |3\rangle$ transitions are no longer effectively isolated. Instead, stronger optical driving enlarges the effective linewidth through power broadening, so that the spectral contributions of the two transitions overlap substantially. This overlap is already visible in Figure 3(a) and becomes more pronounced in Figures 3(b) and 3(c), where the overall spectrum appears increasingly merged into a composite profile. Under this condition, the absorption profile is no longer determined by one dominant near-resonant transition alone, but by the combined steady-state interplay of coherent excitation, relaxation, and redistribution of population among the three states.

It is important to distinguish the spectral merging observed here from electromagnetically induced transparency (EIT), which is commonly discussed in Λ-type systems under a probe–control, or pump–probe, excitation scheme. In a conventional EIT configuration, a weak probe field measures the absorption on one transition, while a second coherent control field couples the other transition and establishes a two-photon dark-state resonance. The present calculation does not correspond to this situation. Both optically allowed transitions are driven by the same monochromatic continuous-wave field, and the calculated quantity is the total steady-state absorption rather than the weak-probe susceptibility in the presence of a separate control field. Although the density-matrix formulation retains the optical coherences, Figure 3 does not exhibit a narrow transparency window or dark-state resonance. Therefore, the strong-field spectral profile is attributed primarily to the overlap of power-broadened absorption channels and relaxation-induced population redistribution, rather than to EIT-type destructive interference.

The effect of γ_{32} also becomes more pronounced in the strong-field regime, as seen from the stronger variation of the broadened spectral profile within each of Figures 3(a)-3(c). Because the upper state is populated more efficiently when the driving field is strong, dissipation affects not only the linewidth but also the balance between the two competing absorption channels. Consequently, increasing γ_{32} modifies the spectral height and width more strongly than in the weak-field case. At the same time, comparison among Figures 3(a)-(c) shows that variation of μ_{32} produces a more evident change in the overall spectral profile than in Figure 2. A larger dipole moment enhances the field-induced coupling of both transitions and strengthens the nonlinear interplay between them. The resulting spectrum therefore reflects a competition between coherent driving and relaxation that is qualitatively different from the weak-field regime, where the two transitions remain more easily distinguishable. In this sense, the single broadened peak in Figure 3 should be interpreted not as a simple resonance of one transition, but as an effective composite response of the two optically allowed pathways.

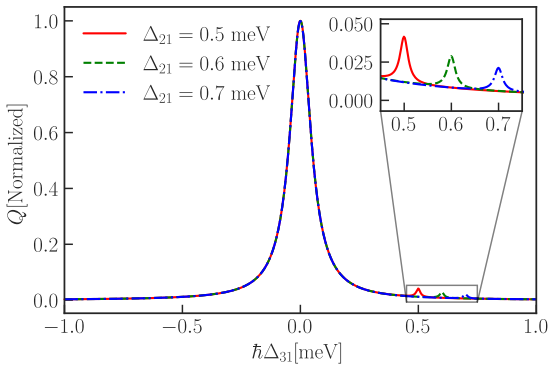


Figure 4. Optical absorption spectrum for $\Omega_{31} = 10^{0.5}\,\gamma_{31}$, $\gamma_{32} = 3\gamma_{31}$, and $\mu_{32} = 0.3\mu_{31}$, with each curve corresponding to a different value of Δ_{21}. The systematic shift of the weak secondary peak with increasing Δ_{21} confirms that this feature originates predominantly from the $|2\rangle \leftrightarrow |3\rangle$ transition.

To verify the physical origin of the weaker feature observed in Figure 2, the splitting energy Δ_{21} is varied while the other parameters are fixed at values that provide the clearest spectral separation,

as shown in Figure 4. Under the condition $\Omega_{31} = 10^{0.5}\gamma_{31}$, $\gamma_{32} = 3\gamma_{31}$, and $\mu_{32} = 0.3\mu_{31}$, each curve in Figure 4 corresponds to a different value of Δ_{21}. The comparison among these curves shows that the secondary peak shifts systematically as Δ_{21} increases, whereas the primary peak remains nearly unchanged. This behavior strongly supports the interpretation that the smaller peak originates predominantly from the $|2\rangle \leftrightarrow |3\rangle$ transition, because changing Δ_{21} directly changes the resonance condition of that transition while leaving the $|1\rangle \leftrightarrow |3\rangle$ transition essentially unaffected. In addition, the secondary peak becomes weaker as Δ_{21} increases. Physically, a larger splitting energy reduces the effectiveness of the indirect population transfer pathway that feeds the $|2\rangle \leftrightarrow |3\rangle$ absorption channel under weak excitation. As a consequence, the steady-state population available to support this secondary transition becomes smaller, and the corresponding absorption feature decreases in magnitude.

The inset of Figure 4 shows that the secondary maxima are located close to the corresponding values of Δ_{21}, namely around 0.5, 0.6, and 0.7 meV. Thus, within the spectral resolution and linewidth of the calculated curves, the secondary peaks follow the resonance condition $\hbar\Delta_{31} \approx \Delta_{21}$. No systematic displacement that can be identified as an AC-Stark-like shift is observed in this weak-field calculation. Small deviations from exact equality, if present, are expected to arise from the finite linewidth of the dissipative steady-state response rather than from a pronounced field-induced level shift.

Taken together, the results in Figures 2–4 show that the absorption spectrum of the isolated Λ-type three-level SQD is governed by different mechanisms in the weak- and strong-field regimes. Under weak excitation, as seen in Figures 2(a)–2(c), the spectrum is dominated by the near-resonant $|1\rangle \leftrightarrow |3\rangle$transition, while the $|2\rangle \leftrightarrow |3\rangle$ contribution appears only as a weaker secondary feature activated through relaxation-assisted population redistribution. Under strong excitation, as shown in Figures 3(a)–3(c), power broadening and stronger coherent coupling enhance the interplay between the two optical channels, so that the final spectral profile is determined by the combined action of transition strength, relaxation, and lower-state splitting. The role of Δ_{21} in determining the position and visibility of the secondary resonance is further confirmed by Figure 4. In this way, the present results clarify how the transition dipole moment and the relaxation rate govern not only the amplitude and linewidth of the absorption spectrum, but also the emergence and merging of multilevel spectral features in an isolated SQD.

It should also be noted that the present calculations adopt a relatively large value of the splitting energy Δ_{21} so that the absorption features associated with the $|1\rangle \leftrightarrow |3\rangle$ and $|2\rangle \leftrightarrow |3\rangle$ transitions can be resolved clearly. This choice is useful for identifying the separate roles of γ_{32} and μ_{32} , but it also implies that relatively strong optical driving is required before the two transitions interact significantly in the strong-field regime. If Δ_{21} is significantly smaller, as may occur in experimental quantum-dot systems, the two resonances would lie closer to each other and may overlap even at lower driving strength. In that case, the secondary feature would be less clearly resolved as a separate peak and would instead appear as a shoulder or as part of a broadened composite absorption profile. However, the underlying mechanism would not change qualitatively: γ_{32} would still provide population redistribution into state $|2\rangle$, μ_{32} would still control the coupling strength of the $|2\rangle \leftrightarrow |3\rangle$ channel, and strong excitation would still promote spectral merging through power broadening and overlap of the two absorption pathways. Therefore, the strong-field results reported here should be interpreted primarily as a mechanism-oriented analysis rather than as a direct quantitative prediction for a specific experimental SQD. In realistic systems, where the lower-state splitting may be considerably smaller, the same qualitative competition between coherent driving and relaxation is still expected, although the field intensity required to observe strong nonlinear spectral modification may be substantially different. This point is consistent with the experimental scale of level splitting reported for semiconductor quantum-dot systems (Brunner et al., 2009). In addition, the present model does not explicitly include pure dephasing. Additional dephasing would increase the decay rates of the optical coherences, broaden the absorption lines, reduce spectral contrast, and further smooth the composite profile in the strong-field regime. Thus, pure dephasing is expected to affect the quantitative linewidth and visibility of the spectral features, but not the qualitative mechanism by which relaxation-assisted population redistribution and power broadening produce the observed line shape.

4. CONCLUSION

This study has theoretically clarified the optical absorption of an isolated Λ-type three-level semiconductor quantum dot under continuous-wave excitation by identifying the roles of the transition dipole moment and the relaxation rate. The results show that the absorption spectrum is governed by different mechanisms in the weak- and strong-field regimes. In the weak-field regime, the response is dominated by the $|1\rangle \leftrightarrow |3\rangle$ transition, while the $|2\rangle \leftrightarrow |3\rangle$ transition appears only as a weaker secondary feature activated through relaxation-assisted population redistribution, as confirmed by the suppression of this feature when the γ_{32} relaxation channel is removed. In this regime, the relaxation rate mainly controls the linewidth and amplitude of the dominant peak, whereas the transition dipole moment more strongly affects the weaker channel. In the strong-field regime, stronger coherent driving and power broadening merge the two absorption pathways into a broadened composite spectral response. Variation of the lower-state splitting further confirms that the secondary resonance originates predominantly from the $|2\rangle \leftrightarrow |3\rangle$ transition. These findings provide a clearer physical picture of how transition strength and dissipation govern the absorption line shape of an elementary multilevel SQD system. The present study is, however, subject to the limitation that a relatively large lower-state splitting was adopted to separate the two absorption channels clearly. Future work should therefore examine more experimentally realistic parameter ranges and include additional effects such as pure dephasing, which may broaden and smooth the composite strong-field profile, as well as excitonic fine structure or coupling to nearby nanostructures. Overall, the present results show that even an isolated Λ-type three-level SQD already exhibits nontrivial multilevel absorption behavior and can serve as a useful baseline for understanding more complex quantum-dot systems.

ACKNOWLEDGEMENT

This work was supported by DIPA UNTAN No. SP DIPA-023.17.2.677517/2023, contract No. 2792/UN22.8/PT.01.05/2024.

REFERENCE

Alivisatos, A. P. (1996). Semiconductor Clusters, Nanocrystals, and Quantum Dots. *Science*, *271*(5251), 933–937. https://doi.org/10.1126/science.271.5251.933

Bayrakli, I. (2021). Electromagnetically induced transparency in natural and artificial molecules. *Optics & Laser Technology*, *141*, 107168. https://doi.org/https://doi.org/10.1016/j.optlastec.2021.107168

Brunner, D., Gerardot, B. D., Dalgarno, P. A., Wüst, G., Karrai, K., Stoltz, N. G., Petroff, P. M., & Warburton, R. J. (2009). A coherent single-hole spin in a semiconductor. *Science*, *325*(5936), 70–72. https://doi.org/10.1126/science.1173684

Chen, X., Liu, Y., & Ma, Q. (2018). Recent advances in quantum dot-based electrochemiluminescence sensors. *Journal of Materials Chemistry C*, *6*(5), 942–959. https://doi.org/10.1039/c7tc05474b

Deng, Y., Lin, X., Fang, W., Di, D., Wang, L., Friend, R. H., Peng, X., & Jin, Y. (2020). Deciphering exciton-generation processes in quantum-dot electroluminescence. *Nature Communications*, *11*(1), 1–8. https://doi.org/10.1038/s41467-020-15944-z

Foerster, A., & Besley, N. A. (2022). Quantum Chemical Characterization and Design of Quantum Dots for Sensing Applications. *The Journal of Physical Chemistry A*, *126*(19), 2899–2908. https://doi.org/10.1021/acs.jpca.2c00947

Gui, X., Lu, Y., Wang, Q., Cai, M., & Sun, S. (2024). Application of Quantum Dots for Photocatalytic Hydrogen Evolution Reaction. *Applied Sciences (Switzerland)*, *14*(12). https://doi.org/10.3390/app14125333

Guo, W., Song, X., Liu, J., Liu, W., Chu, X., & Lei, Z. (2024). Quantum Dots as a Potential Multifunctional Material for the Enhancement of Clinical Diagnosis Strategies and Cancer Treatments. *Nanomaterials*, *14*(13). https://doi.org/10.3390/nano14131088

Holtkemper, M., Reiter, D. E., & Kuhn, T. (2018). Influence of the quantum dot geometry on p -shell transitions in differently charged quantum dots. *Physical Review B*, *97*(7), 1–14. https://doi.org/10.1103/PhysRevB.97.075308

Li, B., Zhang, G., Gao, Y., Chen, X., Chen, R., Qin, C., Hu, J., Wu, R., Xiao, L., & Jia, S. (2024). Single quantum dot spectroscopy for exciton dynamics. *Nano Research*, *17*(12), 10332–10345. https://doi.org/10.1007/s12274-024-6504-x

Maiti, S., Dana, J., & Ghosh, H. N. (2019). Correlating Charge-Carrier Dynamics with Efficiency in Quantum-Dot Solar Cells: Can Excitonics Lead to Highly Efficient Devices? In *Chemistry - A European Journal* (Vol. 25, Issue 3, pp. 692–702). https://doi.org/10.1002/chem.201801853

Marino, E., Sciortino, A., Berkhout, A., MacArthur, K. E., Heggen, M., Gregorkiewicz, T., Kodger, T. E., Capretti, A., Murray, C. B., Femius Koenderink, A., Messina, F., & Schall, P. (2020). Simultaneous photonic and excitonic coupling in spherical quantum dot supercrystals. *ACS Nano*, *14*(10), 13806–13815. https://doi.org/10.1021/acsnano.0c06188

Martynenko, I. V., Litvin, A. P., Purcell-Milton, F., Baranov, A. V., Fedorov, A. V., & Gun'Ko, Y. K. (2017). Application of semiconductor quantum dots in bioimaging and biosensing. *Journal of Materials Chemistry B*, *5*(33), 6701–6727. https://doi.org/10.1039/c7tb01425b

Nugroho, B. S., & Yulyanto. (2020). Analisis Respons Optis Nanokomposit : Pengaruh Faktor Geometris. *POSITRON Berkala Ilmiah Fisika*, *10*(1), 73–79. https://doi.org/10.26418/positron.v10i1.40947

Ollivier, H., Maillette De Buy Wenniger, I., Thomas, S., Wein, S. C., Harouri, A., Coppola, G., Hilaire, P., Millet, C., Lemaître, A., Sagnes, I., Krebs, O., Lanco, L., Loredo, J. C., Antón, C., Somaschi, N., & Senellart, P. (2020). Reproducibility of High-Performance Quantum Dot Single-Photon Sources. *ACS Photonics*, *7*(4), 1050–1059. https://doi.org/10.1021/acsphotonics.9b01805

Ondry, J. C., Philbin, J. P., Lostica, M., Rabani, E., & Alivisatos, A. P. (2021). Colloidal Synthesis Path to 2D Crystalline Quantum Dot Superlattices. *ACS Nano*, *15*(2), 2251–2262. https://doi.org/10.1021/acsnano.0c07202

Osypiw, A. R. C., Lee, S., Jung, S.-M., Leoni, S., Smowton, P. M., Hou, B., Kim, J. M., & Amaratunga, G. A. J. (2022). Solution-processed colloidal quantum dots for light emission. *Materials Advances*, *3*(17), 6773–6790. https://doi.org/10.1039/d2ma00375a

Pan, Z., Rao, H., Mora-Seró, I., Bisquert, J., & Zhong, X. (2018). Quantum dot-sensitized solar cells. *Chemical Society Reviews*, *47*(20), 7659–7702. https://doi.org/10.1039/c8cs00431e

Pang, C., Deng, Y. H., Kheradmand, E., Hagelsieb, L. M., Guo, Y., Cheyns, D., Geiregat, P., Hens, Z., & Van Thourhout, D. (2024). A silicon photonics waveguide-coupled colloidal quantum dot photodiode sensitive beyond 1.6 μm. *APL Photonics*, *9*(6). https://doi.org/10.1063/5.0206386

Pokutnyi, S. I., Ovchinnikov, O. V., & Kondratenko, T. S. (2016). Absorption of light by colloidal semiconductor quantum dots. *Journal of Nanophotonics*, *10*(3), 033506. https://doi.org/10.1117/1.jnp.10.033506

Ryzhov, I. V., Malikov, R. F., Malyshev, A. V., & Malyshev, V. A. (2019). Nonlinear optical response of a two-dimensional quantum-dot supercrystal: Emerging multistability, periodic and aperiodic self-oscillations, chaos, and transient chaos. *Physical Review A*, *100*(3). https://doi.org/10.1103/PhysRevA.100.033820

Ryzhov, I. V., Malikov, R. F., Malyshev, A. V., & Malyshev, V. A. (2021). Quantum metasurfaces of arrays of Λ-emitters for photonic nano-devices. *Journal of Optics (United Kingdom)*, *23*(11), 1–14. https://doi.org/10.1088/2040-8986/ac2788

Shen, H., Gao, Q., Zhang, Y., Lin, Y., Lin, Q., Li, Z., Chen, L., Zeng, Z., Li, X., Jia, Y., Wang, S., Du, Z., Li, L. S., & Zhang, Z. (2019). Visible quantum dot light-emitting diodes with simultaneous high brightness and efficiency. *Nature Photonics*, *13*(3), 192–197. https://doi.org/10.1038/s41566-019-0364-z

Toscano-Negrette, R. G., León-González, J. C., Vinasco, J. A., Morales, A. L., Mora-Ramos, M. E., & Duque, C. A. (2023). Effect of External Fields on the Electronic and Optical Properties in ZnTe/CdSe and CdSe/ZnTe Spherical Quantum Dots. *Condensed Matter*, *8*(3), 1–19. https://doi.org/10.3390/condmat8030066

Vovk, I. A., Tepliakov, N. V., Baimuratov, A. S., Leonov, M. Y., Baranov, A. V., Fedorov, A. V., & Rukhlenko, I. D. (2018). Excitonic phenomena in perovskite quantum-dot supercrystals. *Physical Chemistry Chemical Physics*, *20*(38), 25023–25030. https://doi.org/10.1039/c8cp04724c

Yariv, A. (1989). Quantum Electronics, 3rd. *Edn.(John WieLy & Sons, New York, 1988) P*, *389*.

Yin, N., Liu, L., Li, P., & Zhao, S. (2018). Tunable excitation properties of ZnCdS:Mn/ZnS quantum dots for cancer imaging. *Luminescence*, *33*(3), 630–635. https://doi.org/10.1002/bio.3456

Yücel, M. B., Sari, H., Duque, C. M., Duque, C. A., & Kasapoglu, E. (2022). Theoretical Study of the Exciton Binding Energy and Exciton Absorption in Different Hyperbolic-Type Quantum Wells under Applied Electric, Magnetic, and Intense Laser Fields. *International Journal of Molecular Sciences*, *23*(19). https://doi.org/10.3390/ijms231911429